

Research Article

Stress and Displacement of Deep-Buried Composite Lining Tunnel under Different Contact Conditions

Shuhong Liu ¹, Jiajun Duan,² Jinlu Fan,¹ and Yongquan Zhu ³

¹Engineering Mechanics, Shijiazhuang Tiedao University, Shijiazhuang 050043, China

²Faculty of Engineering and Physical Sciences, University of Southampton, Southampton SO17 1BJ, UK

³School of Civil Engineering, Shijiazhuang Tiedao University, Shijiazhuang 050043, China

Correspondence should be addressed to Shuhong Liu; liush@stdu.edu.cn

Received 9 November 2022; Revised 26 December 2022; Accepted 4 January 2023; Published 23 January 2023

Academic Editor: Gregory Chagnon

Copyright © 2023 Shuhong Liu et al. This is an open access article distributed under the Creative Commons Attribution License, which permits unrestricted use, distribution, and reproduction in any medium, provided the original work is properly cited.

Stress and displacement of the composite lining are important factors to be considered during tunnel design. By the complex variable method, analytical solutions for stress and displacement of surrounding rock, primary support and secondary lining satisfying the interface continuity and boundary conditions under far-field stresses are derived. Taking the railway composite lining tunnel as an example, the analytical distributions of stress and displacement along boundaries are given, which was in good agreement with the numerical solution calculated by finite element software. The results show that the maximum normal stress ratio (load sharing ratio) of the outer boundary between the secondary lining and the primary support is 0.74. The radial displacement of the inner boundary of surrounding rock, primary support, and secondary lining change consistently. The maximum settlement and uplift occur at the vault and bottom, respectively. The tangential stress of secondary lining is compressive stress, while the tangential stress of primary support is tensile stress and compressive stress. The maximum tangential stress of primary support and secondary lining is smaller than the allowable stress of concrete.

1. Introduction

The complex variable function is the most effective method to solve deep-buried tunnel problems. Obtaining the conformal mapping function of the tunnel is the critical step when solving the mechanical response. The conformal mapping functions of unlined tunnels can be obtained by different methods. Lu [1] and Wang [2] obtained the conformal mapping function of noncircular tunnels with a single lining.

Exadaktylos and Stavropoulou [3], Exadaktylos et al. [4], and Guan et al. [5] obtained analytical solutions for stress and displacement of rock mass around unlined tunnels with different cross sections. Based on the analytical stress and displacement distribution, Xu et al. [6], Ma et al. [7–9], and Liu et al. [10, 11] studied plastic zones around tunnels with circular, elliptical, and horseshoe-shaped cross sections, respectively; Wu et al. [12] clarified failure mechanism of horseshoe-shaped tunnel; Liu et al. [13] studied viscoelastic

displacements of a noncircular tunnel by using the elastic-viscoelastic correspondence principle.

For circular tunnels with single-layer lining, Wang and Li [14] obtained stress and displacement around a circular tunnel at great depth subjected to uniform internal pressure and unequal biaxial in situ stresses. Li et al. [15] deduced the elastic-plastic analytical solution for the stress and displacement of circular tunnel subjected to uniform internal and external pressure. Kargar [16] proposed analytical solutions around lined and unlined circular tunnels in viscous rock mass. Guo et al. [17] studied the stress, displacement, and stability of a deep lined circular pressure tunnel by combining the complex variable method with the Biot theory. For noncircular tunnels with single-layer lining, Kargar et al. [18, 19] and Lu et al. [20] investigated analytical stress solutions of inverted U-shaped tunnels according to different contact conditions between rock mass and lining, respectively; analytical displacement solutions were also given by Lu et al. [21] and Wang et al. [22] in the isotropic

and orthotropic rock mass, respectively. Li and Chen [23, 24] and Liu et al. [25] obtained the analytical solutions for stress and displacement around horseshoe-shaped tunnels in the isotropic and orthotropic rock mass, respectively. Chen et al. [26] and Fang et al. [27] obtained analytic solutions of two circular and multiple noncircular tunnels at great depth considering the mutual interaction between linings and rock mass, respectively.

Zhou and Yang [28] and Zhou et al. [29, 30] calculated the support loads of circular composite lining tunnels consisting of primary support and secondary lining in elastic and rheological rock mass, respectively. Li et al. [31] proposed the analytical stress solution of circular water conveyance tunnel with composite lining subjected to uniform internal pressure. Ramadan et al. [32], Maleska and Beben [33], and Embaby et al. [34] analysed numerically large-span culverts and soil-steel bridges. Maleska et al. [35], Maleska and Beben [36], Shen et al. [37], Jiang et al. [38], and Chen et al. [39] obtained numerical seismic response of soil-steel bridges, a shield tunnel, and subway stations.

For noncircular tunnels, it can be seen from the above literature that there are many theoretical research results for unlined tunnels and single-layer lining tunnels, while there are few research results for composite lining tunnels widely used in practice. In this paper, the analytical solutions of stress and displacement of surrounding rock, primary support, and secondary lining of the noncircular composite lining tunnel are derived by using the complex variable function method and verified by finite element software ANSYS, which provides a theoretical basis for safe and economical tunnel design.

2. Conformal Mapping Function of Composite Lining Tunnel

Figure 1(a) shows the load structure diagram of a composite lining tunnel with noncircular cross sections, where R , L_1 , and L_2 represent the area of surrounding rock, primary support, and secondary lining, respectively. According to the theory of elastic mechanics, deep-buried tunnels can be simplified as a plane strain model with holes in infinite surrounding rock. Assuming that the buried depth is deep enough, the effect of gravity can be neglected. The surrounding rock is subjected to far-field stresses P and λP along Ox - and Oy -axes, respectively, and λ is the lateral pressure coefficient.

The conformal mapping function of the composite lining tunnel is

$$z = \omega(\zeta) = \sum_{k=1}^m C_k \zeta^{-(k-2)}, \quad (1)$$

where $z = x + iy$, $\zeta = \rho \exp^{i\theta}$, x and y are the rectangular coordinates in the physical z plane, and ρ and θ are the polar coordinates in the image ζ plane. The three concentric circles with radius $\rho=1$, R_1 , and R_2 in the image ζ plane are transformed into the outer boundary of primary support, the inner boundary of primary support (the outer boundary of secondary lining), and the inner boundary of secondary

lining, respectively, as shown in Figure 1(b). m is the number of terms of the conformal mapping function. C_k , R_1 , and R_2 are the coefficients related to the shape and size of the composite lining, which can be solved by Fan [40].

3. Basic Equations

The stress and displacement components of surrounding rock and composite lining are obtained by stress functions. The stress functions of surrounding rock, primary support, and secondary lining and the stress and displacement components in both Cartesian and curvilinear coordinates are given.

3.1. Stress Functions. The stress functions $\phi_1(\zeta)$ and $\psi_1(\zeta)$ of surrounding rock can be expressed as follows:

$$\phi_1(\zeta) = B\omega(\zeta) + \varphi_0(\zeta), \quad (2)$$

$$\psi_1(\zeta) = (B' + iC')\omega(\zeta) + \psi_0(\zeta), \quad (3)$$

where constants B , B' , and C' are related to far-field stress P and λP , $B = P(1 + \lambda)/4$, $B' = -P(1 - \lambda)/2$, $C' = 0$, and the functions $\varphi_0(\zeta)$ and $\psi_0(\zeta)$ are analytic outside the unit circle in the ζ plane and can be written as follows:

$$\begin{aligned} \phi_0(\zeta) &= \sum_{j=0}^n a_j \zeta^{-j}, \\ \psi_0(\zeta) &= \sum_{j=0}^n b_j \zeta^{-j}. \end{aligned} \quad (4)$$

The stress functions $\phi_2(\zeta)$ and $\psi_2(\zeta)$ of primary support are analytic in the annular region with radius $R_1 \leq \rho \leq 1$ in the ζ image plane. The stress functions $\phi_3(\zeta)$ and $\psi_3(\zeta)$ of secondary lining are analytic in the annular region with radius $R_2 \leq \rho \leq R_1$ in the ζ image plane. They can be written as the following series expansions:

$$\phi_2(\zeta) = \sum_{j=1}^n d_j \zeta^{-j} + \sum_{j=0}^n f_j \zeta^j, \quad (5)$$

$$\psi_2(\zeta) = \sum_{j=1}^n g_j \zeta^{-j} + \sum_{j=0}^n h_j \zeta^j,$$

$$\phi_3(\zeta) = \sum_{j=1}^n p_j \zeta^{-j} + \sum_{j=0}^n q_j \zeta^j, \quad (6)$$

$$\psi_3(\zeta) = \sum_{j=1}^n s_j \zeta^{-j} + \sum_{j=0}^n t_j \zeta^j,$$

where $10n + 6$ unknown real coefficients a_j , b_j , d_j , f_j , g_j , h_j , p_j , q_j , s_j , and t_j can be determined by the interface continuity and boundary conditions.

3.2. Stresses and Displacements. The stress components are σ_x , σ_y , and τ_{xy} ; the displacement components u_x and u_y in the Cartesian coordinates xoy can be expressed as follows:

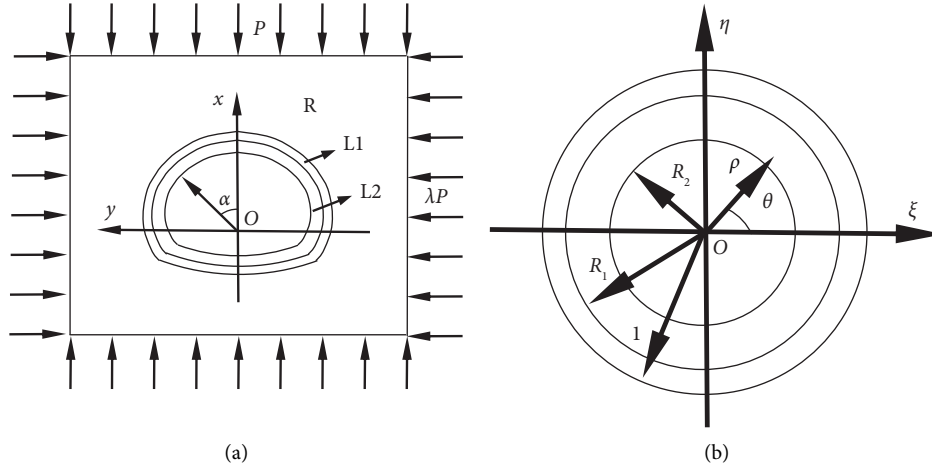


FIGURE 1: Conformal mapping of the composite lining tunnel. (a) Schematic diagram of the tunnel in the physical z plane. (b) Three concentric circles in the image ζ plane.

$$\sigma_x + \sigma_y = 4\text{Re}[\Phi(\zeta)], \quad (7)$$

$$\sigma_y - \sigma_x + 2i\tau_{xy} = \frac{2}{\omega'(\zeta)} \left[\overline{\omega(\zeta)}\Phi'(\zeta) + \omega'(\zeta)\Psi(\zeta) \right], \quad (8)$$

$$2G(u_x + iu_y) = \kappa\phi(\zeta) - \frac{\omega(\zeta)}{\omega'(\zeta)}\overline{\phi'(\zeta)} - \overline{\psi(\zeta)}, \quad (9)$$

where the notation $\Phi(\zeta) = \phi'(\zeta)/\omega'(\zeta)$ and $\Psi(\zeta) = \psi'(\zeta)/\omega'(\zeta)$ are introduced for simple expression. $\phi(\zeta)$ and $\psi(\zeta)$ are the stress functions. Constant $\kappa = 3 - 4\mu$ for plane strain problem, the shear modulus $G = E/2(1 + \mu)$, and E and μ is Young's modulus and Poisson's ratio, respectively.

The stress and displacement components in the curved coordinates are as follows:

$$\sigma_\rho + \sigma_\theta = 4\text{Re}[\Phi(\zeta)], \quad (10)$$

$$\sigma_\rho - \sigma_\theta + 2i\tau_{\rho\theta} = \frac{2\zeta^2}{\rho^2\omega'(\zeta)} \left[\overline{\omega(\zeta)}\Phi'(\zeta) + \omega'(\zeta)\Psi(\zeta) \right], \quad (11)$$

$$u_\rho + iu_\theta = \frac{1}{2G} \frac{\bar{\zeta}}{\rho} \frac{\overline{\omega'(\zeta)}}{|\omega'(\zeta)|} \left[\kappa\phi(\zeta) - \frac{\omega(\zeta)}{\omega'(\zeta)}\overline{\phi'(\zeta)} - \overline{\psi(\zeta)} \right], \quad (12)$$

where σ_ρ , σ_θ , and $\tau_{\rho\theta}$ are the radial, tangential, and shear stress components, respectively; u_ρ and u_θ are the radial and tangential displacements, respectively.

The stress functions $\phi(\zeta)$ and $\psi(\zeta)$ in equations (7)–(12) are replaced by $\phi_1(\zeta)$ and $\psi_1(\zeta)$ for surrounding rock, $\phi_2(\zeta)$ and $\psi_2(\zeta)$ for primary support, and $\phi_3(\zeta)$ and $\psi_3(\zeta)$ for secondary lining. The shear modulus G and constant κ in equations (9) and (12) are replaced by shear modulus G_1 and κ_1 of surrounding rock, G_2 and κ_2 of primary lining, and G_3 and κ_3 of secondary lining. Then, the stress and displacement components of surrounding rock, primary support, and secondary lining can be obtained.

The relationship between surface force and stress functions is as follows:

$$\phi(\zeta) - \frac{\omega(\zeta)}{\omega'(\zeta)}\overline{\phi'(\zeta)} - \overline{\psi(\zeta)} = i \int (\overline{f_x} + i\overline{f_y}) ds, \quad (13)$$

where $\overline{f_x}$ and $\overline{f_y}$ are the surface force components in x and y directions, respectively.

4. Continuity and Boundary Conditions

The surface between surrounding rock and primary support $\zeta (= \exp^{i\theta} = \sigma)$ is assumed to be full contact. The corresponding stress and displacement components are equal, respectively [18, 19, 25]. From equations (9) and (13), the interface continuity conditions can be written as follows:

$$\frac{\left[\kappa_1\phi_1(\sigma) - \frac{\omega(\sigma)}{\omega'(\sigma)}\overline{\phi_1'(\sigma)} - \overline{\psi_1(\sigma)} \right]}{G_1} = \frac{\left[\kappa_2\phi_2(\sigma) - \frac{\omega(\sigma)}{\omega'(\sigma)}\overline{\phi_2'(\sigma)} - \overline{\psi_2(\sigma)} \right]}{G_2}, \quad (14)$$

$$\phi_1(\sigma) - \frac{\omega(\sigma)}{\omega'(\sigma)}\overline{\phi_1'(\sigma)} - \overline{\psi_1(\sigma)} = \phi_2(\sigma) - \frac{\omega(\sigma)}{\omega'(\sigma)}\overline{\phi_2'(\sigma)} - \overline{\psi_2(\sigma)}. \quad (15)$$

Because the waterproof layer between primary support and secondary lining cannot bear the shear force, this interface ($\zeta = R_1\sigma$) is assumed to be slip contact. The corresponding normal displacement and stress are equal,

$$\operatorname{Re} \left\{ \frac{\overline{\sigma\omega'(R_1\sigma)}}{G_2} \left[\kappa_2 \phi_2(R_1\sigma) - \frac{\omega(R_1\sigma)}{\omega'(R_1\sigma)} \overline{\phi_2'(R_1\sigma) - \psi_2(R_1\sigma)} \right] \right\} = \operatorname{Re} \left\{ \frac{\overline{\sigma\omega'(R_1\sigma)}}{G_3} \left[\kappa_3 \phi_3(R_1\sigma) - \frac{\omega(R_1\sigma)}{\omega'(R_1\sigma)} \overline{\phi_3'(R_1\sigma) - \psi_3(R_1\sigma)} \right] \right\}. \quad (16)$$

From equations (11) and (12), the stress continuity condition can be expressed as follows:

$$\operatorname{Im} \left\{ \frac{\sigma^2}{\omega'(R_1\sigma)} \left[\overline{\omega(R_1\sigma)\Phi_3'(R_1\sigma) + \omega'(R_1\sigma)\Psi_3(R_1\sigma)} \right] \right\} = 0, \quad (17)$$

$$\phi_2(R_1\sigma) - \frac{\omega(R_1\sigma)}{\omega'(R_1\sigma)} \overline{\phi_2'(R_1\sigma) - \psi_2(R_1\sigma)} = \phi_3(R_1\sigma) - \frac{\omega(R_1\sigma)}{\omega'(R_1\sigma)} \overline{\phi_3'(R_1\sigma) - \psi_3(R_1\sigma)}. \quad (18)$$

The inner boundary of secondary lining ($\zeta = R_2\sigma$) is free; the radial stress and tangent stress are equal to 0. From equation (12), the stress boundary condition is as follows:

$$\phi_3(R_2\sigma) - \frac{\omega(R_2\sigma)}{\omega'(R_2\sigma)} \overline{\phi_3'(R_2\sigma) - \psi_3(R_2\sigma)} = 0. \quad (19)$$

5. Solution Process of Stress Function

By applying series solution to solve unknown coefficients a_j , b_j , d_j , f_j , g_j , h_j , p_j , q_j , s_j , and t_j of stress functions, the stress and displacement components can be obtained.

In order to ensure the accuracy of the results, $\omega(\sigma)/\omega'(\sigma)$, $\omega(R_1\sigma)/\omega'(R_1\sigma)$, and $\omega(R_2\sigma)/\omega'(R_2\sigma)$ in equations (14)–(18)

respectively, and the shear stress is equal to 0. From equation (12), the displacement continuity condition can be expressed as follows:

need to be expanded to a sufficient number of terms. From equations (2) and (5), the minimum exponent of $\phi_1'(\sigma)$ and $\phi_2'(\sigma)$ in equations (14) and (15) is 0 and $-(n-1)$, respectively. In order to multiply them by the maximum exponent of $\omega(\sigma)/\omega'(\sigma)$ to n , the positive exponent term of $\omega(\sigma)/\omega'(\sigma)$ should be $2n-1$, and the expansion is as follows:

$$\frac{\omega(\sigma)}{\omega'(\sigma)} = \sum_{j=1}^{m-2} W_j \sigma^{-j} + \sum_{j=0}^{2n-1} W_j' \sigma^j, \quad (20)$$

where W_j and W_j' are the known constants related to C_k [10, 11, 13].

Similarly, $\omega(R_1\sigma)/\omega'(R_1\sigma)$ and $\omega(R_2\sigma)/\omega'(R_2\sigma)$ are expanded as follows:

$$\frac{\omega(R_1\sigma)}{\omega'(R_1\sigma)} = \sum_{j=1}^{m-2} M_j \sigma^{-j} + \sum_{j=0}^{2n-1} M_j' \sigma^j, \quad \frac{\omega(R_2\sigma)}{\omega'(R_2\sigma)} = \sum_{j=1}^{m-2} L_j \sigma^{-j} + \sum_{j=0}^{2n-1} L_j' \sigma^j, \quad (21)$$

where M_j , M_j' , L_j , and L_j' are the known constants related to C_k , R_1 , and R_2 .

Substituting stress functions into continuity and boundary conditions and equaling multipliers of the same order of variables, $2n+1$, $2n+1$, $n+1$, n , $2n+1$, and $2n+1$ equations are obtained from equations (14)–(19),

respectively. Thus, a total of $10n+5$ equations is obtained. But there is a total of $10n+6$ unknown coefficients, and an equation must be added.

The displacement of the inner boundary of surrounding rock caused by tunnel excavation can be written as follows [25]:

$$\frac{\left[\kappa_1 \phi_0(\sigma) - \omega(\sigma)/\omega'(\sigma) \overline{\phi_0'(\sigma) - \psi_0(\sigma)} \right]}{2G_1} = \frac{\left[-\left(\sum_{j=1}^{m-2} W_j \sigma^{-j} + \sum_{j=0}^{2n-1} W_j' \sigma^j \right) \sum_{j=1}^n j a_j \sigma^{j+1} + \kappa_1 \sum_{j=0}^n a_j \sigma^{-j} - \sum_{j=0}^n b_j \sigma^j \right]}{2G_1}. \quad (22)$$

The displacement at infinity caused by tunnel excavation is equal to 0, that is, the constant term in the right side of equation (22) is 0. Since the minimum positive exponent term of $\overline{\phi_0'(\sigma)}$ is σ^2 , the maximum negative exponent term of $\omega(\sigma)/\overline{\omega'(\sigma)}$ is σ^{-2} . The supplementary equation is expressed as follows:

$$\kappa_1 a_0 - \sum_{k=2}^{m-2} W_k (k-1) a_{k-1} + b_0 = 0. \quad (23)$$

6. Results and Discussion

Taking the double-line railway composite lining tunnel in grade IV surrounding rock as an example, the analytical distributions of stress and displacement along boundaries are given and compared with the numerical distributions. The primary support is made of C25 concrete with a thickness of 0.25 m, and the secondary lining is made of C35 concrete with a thickness of 0.45 m. The material parameters of surrounding rock, primary support, and secondary lining are as follows: Young's elastic modules: $E_1 = 3.7$ Gpa, $E_2 = 23$ Gpa, and $E_3 = 31.5$ Gpa; and Poisson's ratios: $\mu_1 = 0.325$, $\mu_2 = 0.2$, and $\mu_3 = 0.2$, respectively. The vertical infinity pressure $P = 0.148762$ Mpa, and the lateral pressure coefficient $\lambda = 0.2$ [41].

6.1. Conformal Mapping Function. The conformal mapping function of composite lining tunnel is obtained as follows: $\omega(\zeta) = 0.7268/\zeta + 6.7015 - 0.5140\zeta + 0.2968\zeta^2 - 0.1282\zeta^3 + 0.0290\zeta^4 + 0.0105\zeta^5 - 0.0152\zeta^6 + 0.0083\zeta^7 - 0.0024\zeta^8 - 0.0002\zeta^9 + 0.0001\zeta^{10} - 0.0004\zeta^{11} + 0.0009\zeta^{12}$ and $R_1 = 0.9632$ and $R_2 = 0.8975$. The composite lining after transformation is shown in Figure 2.

6.2. Comparison of Analytical Solution with Numerical Solution. In order to verify the correctness of the above analytical solution, the finite element software ANSYS is used for numerical simulation, and the analytical solution of stress and displacement is compared with the numerical solution. The composite lining adopts the transformed shape. Because the structure and load are symmetrical, the left half structure is adopted. The size of the plane strain model is $180\text{ m} \times 360\text{ m}$, far greater than the size of the tunnel. The upper, left, and lower boundaries are free, and normal constraints are imposed on the right boundary. The upper and lower boundaries apply pressure of 0.148762 Mpa, and the left boundary applies pressure of 0.0297524 Mpa. The above measures ensure that the model, boundary conditions, and loads in the numerical solution are consistent with those in the analytical solution, thus ensuring the comparability of the two solutions. Because the model is large and the mesh is dense, the finite element mesh of surrounding rock near the tunnel is shown in Figure 3(a), with a total of 24516 units and 49573 nodes. The primary support grid is shown in Figure 3(b), with 1140 elements and 2286 nodes. The secondary lining grid is shown in Figure 3(c), with 1484 elements and 3333 nodes. The contact

surfaces of surrounding rock, primary support, and secondary lining are full contact and slip contact, respectively. Slip contact is realized by establishing contact pairs, which are composed of target surface and contact surface. The contact type is nonseparation contact, and the friction coefficient is zero.

Figures 4(a) and 4(b) show the contours of stress σ_x and displacements u_x around the tunnel, respectively. It can be seen that stress σ_x changes obviously in the composite lining and gradually approaches the applied load of 0.148762 Mpa at a distance from the tunnel in surrounding rock. The displacement u_x changes consistently. The changes of stress and displacement of surrounding rock are mainly concentrated near the tunnel.

It is convenient to read the calculation results under the rectangular coordinate system in the finite element software ANSYS. In order to clearly see the difference between the numerical solution and the analytical solution, as an example, Figures 5(a) and 5(b) show the numerical solution and the analytical solution of the stress and displacement of the inner boundary of secondary lining ($\rho = 0.8975$). A positive angle α turns counterclockwise from the positive x -axis to the positive y -axis (Figure 1(a)). The analytical solution is calculated by taking $n = 100$ in this study. From Figure 5(a), it can be seen that the numerical solution and the analytical solution of stresses $\sigma_x^{L_2}$ and $\sigma_y^{L_2}$ are almost identical. When $\alpha = 0^\circ$ and 180° , the stress $\sigma_x^{L_2}$ is zero, satisfying the boundary condition. From Figure 5(b), it can be seen that the numerical solution and the analytical solution of the displacement $u_x^{L_2}$ are almost identical. While, there is a small rigid body translation for the displacement $u_x^{L_2}$ because the finite element model has no constraints in the vertical direction. When $\alpha = 0^\circ$ and 180° , the displacement $u_y^{L_2}$ is zero, satisfying the symmetry condition.

6.3. Analytical Distributions of Stress and Displacement along Boundaries. The analytical distributions of stress and displacement along boundaries are given, in order to verify the continuity conditions and boundary conditions and find the maximum stress and displacement.

On the interface between surrounding rock and primary support ($\rho = 1$), the radial stresses $\sigma_\rho^R, \sigma_\rho^{L_1}$, shear stresses $\tau_{\rho\theta}^R, \tau_{\rho\theta}^{L_1}$, the radial displacements $u_\rho^R, u_\rho^{L_1}$, and tangential displacements $u_\theta^R, u_\theta^{L_1}$ of the inner boundary of surrounding rock and the outer boundary of primary support are shown in Figures 6(a) and 6(b), respectively. It can be seen that the corresponding stress and displacement are equal to satisfy the full contact condition. The radial stress is all compressive, and the maximum value of 0.146 MPa occurs at point A (Figure 2).

On the interface between primary support and secondary lining ($\rho = 0.9632$), the radial stresses $\sigma_\rho^{L_1}, \sigma_\rho^{L_2}$ and shear stresses $\tau_{\rho\theta}^{L_1}, \tau_{\rho\theta}^{L_2}$ and the radial displacements $u_\rho^{L_1}, u_\rho^{L_2}$ and tangential displacements $u_\theta^{L_1}, u_\theta^{L_2}$ of the inner boundary of primary support and the outer boundary of secondary lining are shown in Figures 7(a) and 7(b), respectively. The corresponding radial stress is equal, while the shear stress is zero. The corresponding radial displacement is equal, while

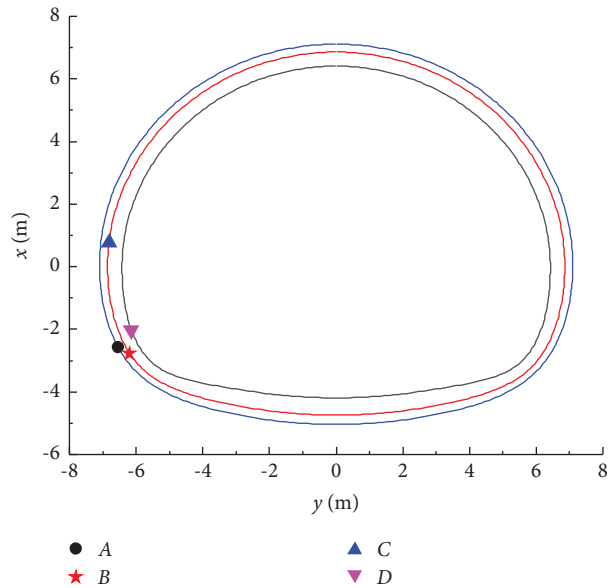


FIGURE 2: Composite lining after transformation.

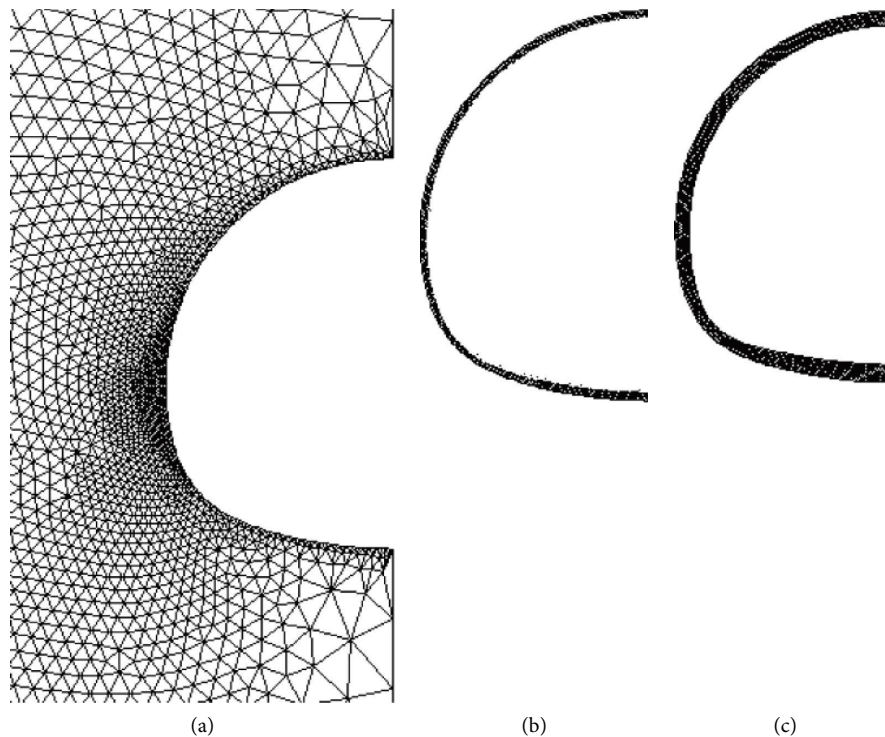


FIGURE 3: Finite element mesh. (a) Surrounding rock. (b) Primary support. (c) Secondary lining.

the corresponding tangential displacement is not equal. From these results, it can be seen that the slip contact condition is satisfied. The radial stress is compressive stress, and the maximum value of 0.108 MPa occurs at point B (Figure 2). The load sharing ratio concerned in the design, that is, the maximum normal stress ratio of the outer boundary between the secondary lining and the primary support is 0.74.

The radial stress $\sigma_{\rho}^{L_2}$ and shear stress $\tau_{\rho\theta}^{L_2}$ and the radial displacement $u_{\rho}^{L_2}$ and tangential displacement $u_{\theta}^{L_2}$ of the inner boundary of secondary lining ($\rho = 0.8975$) are shown in Figures 8(a) and 8(b), respectively. Since the radial stress and shear stress are equal to zero, the stress boundary conditions are satisfied.

From Figures 6–8, it can be seen that the stress change trend is different on each boundary, while the radial

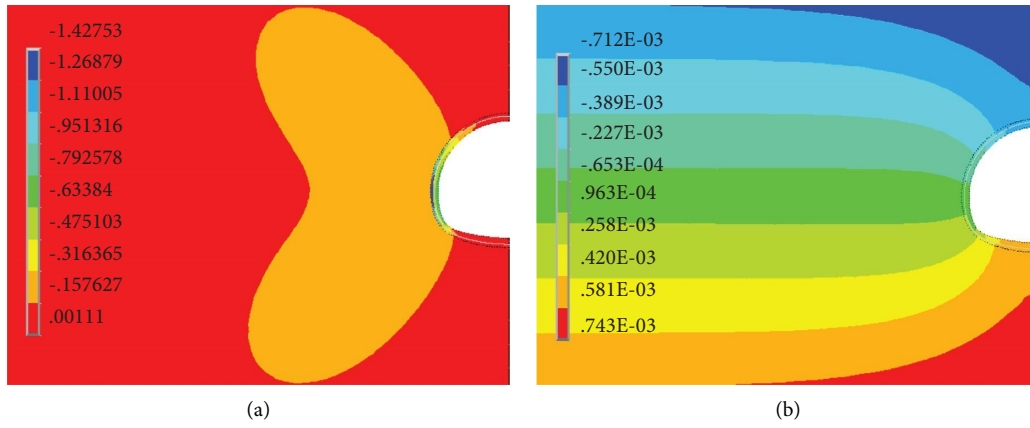


FIGURE 4: Stress and displacement contours. (a) Stress σ_x . (b) Displacement u_x .

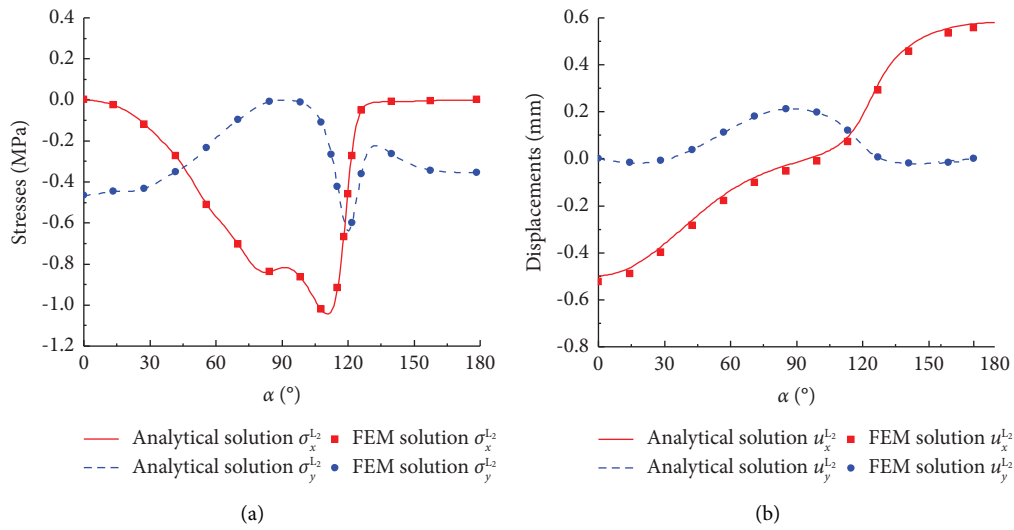


FIGURE 5: Analytical and numerical solutions ($\rho=0.8975$). (a) Stresses. (b) Displacements.

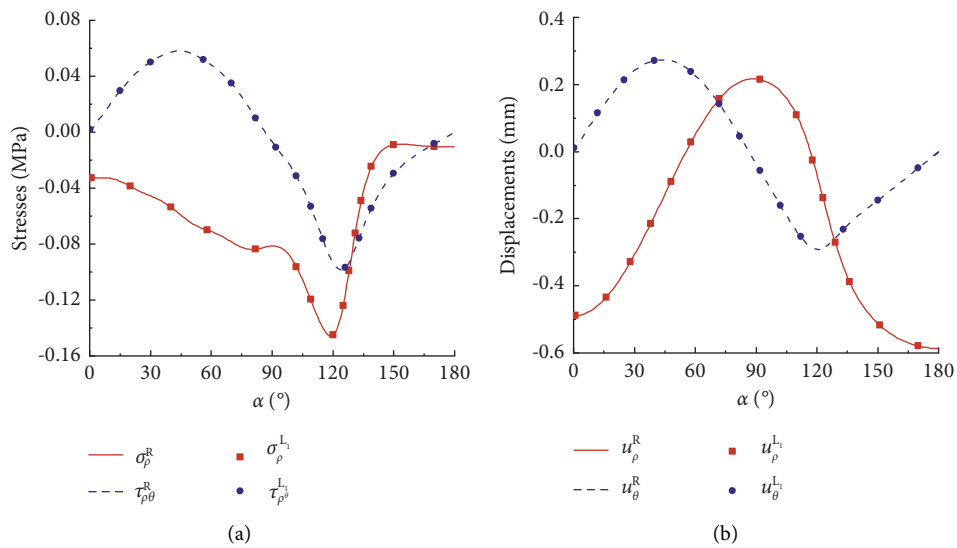


FIGURE 6: Distributions on the interface between surrounding rock and primary support. (a) Stresses. (b) Displacements.

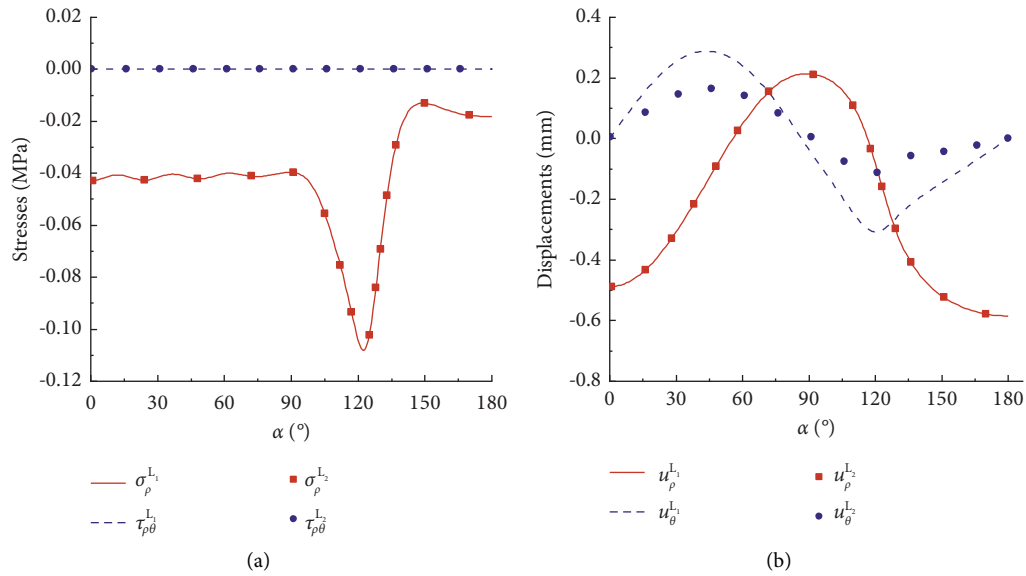


FIGURE 7: Distributions on the interface between primary support and secondary lining. (a) Stresses. (b) Displacements.

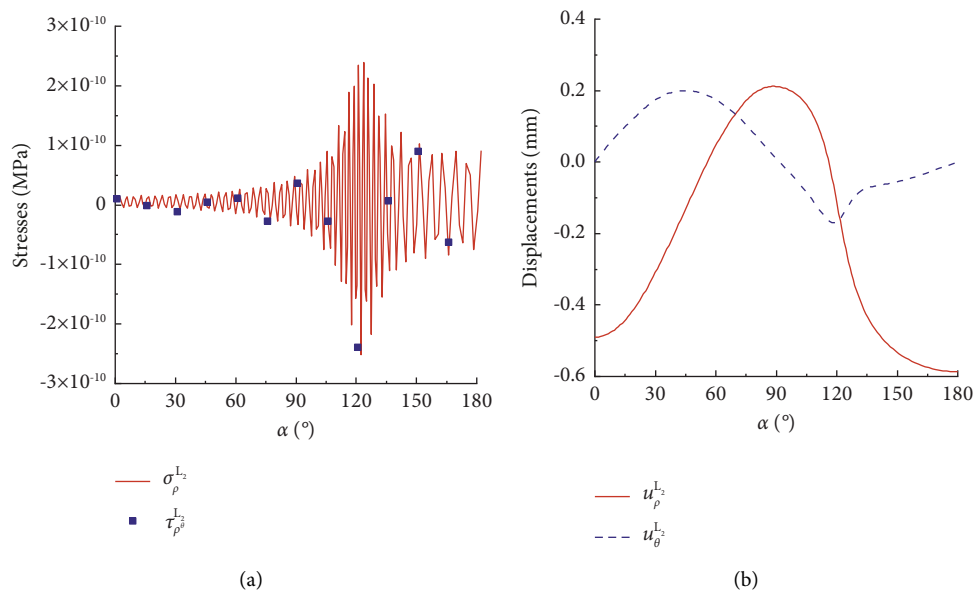


FIGURE 8: Distributions on the inner boundary of secondary lining. (a) Stresses. (b) Displacements.

displacement change trend is consistent. The maximum settlement, uplift, and peripheral displacement occur at the vault, bottom, and waist, respectively. On the vertical axis, the shear stress and tangential displacement are equal to zero, satisfying the symmetry condition.

Figure 9 shows the tangential stress of the inner boundary of surrounding rock ($\rho=1$), the inner and outer boundaries of primary support ($\rho=1$ and $\rho=0.9632$), and the inner and outer boundaries of secondary lining ($\rho=0.9632$ and $\rho=0.8975$), respectively. The tangential stress σ_θ^R value of the inner boundary of surrounding rock is the smallest. For composite lining, the maximum compressive stress and tensile stress occur at the inner boundary

of primary support. The maximum compressive stress is 1.425 MPa at point C (Figure 2), and the maximum tensile stress is 0.472 MPa at the bottom. The maximum values of compressive stress and tensile stress are much smaller than the allowable compressive design strength of 13 MPa and tensile design strength of 1.3 MPa of C25 shotcrete [41]. The tangential normal stress $\sigma_\theta^{L_2}$ of secondary lining is compressive stress, and the maximum compressive stress is 1.338 MPa at point D (Figure 2) of the inner boundary of secondary lining, which is much smaller than the allowable compressive stress of 13 MPa of C35 concrete [41]. Therefore, the thickness of primary support and secondary lining can be appropriately reduced.

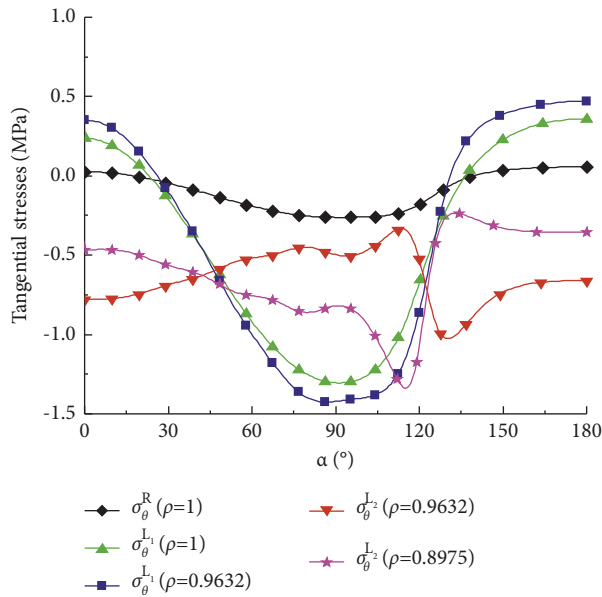


FIGURE 9: Tangential stress distributions along boundaries.

7. Conclusion

According to the complex variable function method, the analytical solutions for stress and displacement of composite lining tunnel are obtained, and compared with the numerical solutions obtained by finite element software, the results are in good agreement. The main conclusions are as follows:

- (1) On the contact surface between surrounding rock and primary support, the corresponding radial stress, shear stress, radial displacement, and tangential displacement of the inner boundary of surrounding rock and the outer boundary of primary support are equal, respectively, which satisfy the full contact condition. On the contact surface between primary support and secondary lining, the corresponding radial stress and displacement of the inner boundary of primary support and the outer boundary of secondary lining are equal, respectively, and the shear stress is zero, which satisfies the slip contact condition. The radial stress and shear stress of the inner boundary of secondary lining are both zero, which satisfies the stress boundary condition. The shear stress and horizontal displacement on the vertical axis are zero, satisfying the symmetry condition.
- (2) The maximum normal stress ratio (load sharing ratio) of the outer boundary between the secondary lining and the primary support is 0.74. The maximum compressive and tensile tangential stress occur at the inner boundary of primary support and the maximum compressive tangential stress of secondary lining occurs at the arch foot of inner boundary. Since they are far less than the allowable stress of concrete, the thickness of primary support and

secondary lining can be appropriately reduced from an economic point of view.

- (3) The radial displacement change trend of surrounding rock, primary support, and secondary lining is consistent. The maximum settlement, uplift, and peripheral displacement occur at the vault, bottom, and waist, respectively. Therefore, during the design and construction of the tunnel, attention should be paid to these locations.

Subsequently, we will combine the on-site monitoring of specific projects to verify the applicability of our solutions, so as to better guide the safe and economical tunnel design.

Data Availability

The data used to support the findings of this study are included within the article.

Conflicts of Interest

The authors declare that they have no conflicts of interest.

Acknowledgments

The work was financially supported by the Natural Science Foundation of China (51778380) and China State Railway Group Co., Ltd. (N2020G040).

References

- [1] A. Lu, "A new method of determination of the mapping function for a non-circle tunnel with full support," *Chinese Journal of Rock Mechanics and Engineering*, vol. 17, no. 4, pp. 38–44, 1995.
- [2] Z. Wang, *Complex Variable Function Solution of Deep Buried Tunnel Excavation*, Shijiazhuang Tiedao University, Shijiazhuang, China, 2018.
- [3] G. Exadaktylos and M. Stavropoulou, "A closed-form elastic solution for stresses and displacements around tunnels," *International Journal of Rock Mechanics and Mining Sciences*, vol. 39, no. 7, pp. 905–916, 2002.
- [4] G. Exadaktylos, P. Liolios, and M. Stavropoulou, "A semi-analytical elastic stress–displacement solution for notched circular openings in rocks," *International Journal of Solids and Structures*, vol. 40, no. 5, pp. 1165–1187, 2003.
- [5] Z. Guan, T. Deng, H. Huang, and Y. Jiang, "Back analysis technique for mountain tunneling based on the complex variable solution," *International Journal of Rock Mechanics and Mining Sciences*, vol. 59, pp. 15–21, 2013.
- [6] M. F. Xu, S. C. Wu, Y. T. Gao, J. Ma, and Q. L. Wu, "Analytical elastic stress solution and plastic zone estimation for a pressure-relief circular tunnel using complex variable methods," *Tunnelling and Underground Space Technology*, vol. 84, pp. 381–398, 2019.
- [7] Y. Ma, A. Lu, H. Cai, and X. Zeng, "A semi-analytical method for elastic-plastic analysis of a deep-buried elliptical tunnel," *Computers and Geotechnics*, vol. 142, Article ID 104589, 2022.
- [8] Y. Ma, A. Lu, X. Zeng, and H. Cai, "Analytical solution for determining the plastic zones around twin circular tunnels excavated at great depth," *International Journal of Rock Mechanics and Mining Sciences*, vol. 136, Article ID 104475, 2020.

- [9] Y. Ma, A. Lu, H. Cai, and X. Zeng, "Analytical solution for determining the plastic zones around two unequal circular tunnels," *Tunnelling and Underground Space Technology*, vol. 120, p. 104267, 2022.
- [10] S. Liu, J. Fan, and Y. Zhu, "Stress and plastic zone of surrounding rock in non-circular unlined tunnel," *China Railway Science*, vol. 43, no. 3, pp. 78–85, 2022.
- [11] S. Liu, J. Fan, C. Wu, and Y. Zhu, "Elastic stress and plastic zone distributions around a deeply buried tunnel under the nonhydrostatic pressure," *Geofluids*, vol. 2022, Article ID 23663291, 10 pages, 2022.
- [12] H. Wu, G. Y. Zhao, and S. W. Ma, "Failure behavior of horseshoe-shaped tunnel in hard rock under high stress: phenomenon and mechanisms," *Transactions of Nonferrous Metals Society of China*, vol. 32, no. 2, pp. 639–656, 2022.
- [13] S. Liu, J. Fan, Z. Chen, and Y. Zhu, "Analytical solution to elastic and viscoelastic displacements for rock mass caused by excavation of deep-buried non-circular tunnel," *Journal of the China Railway Society*, vol. 44, no. 3, pp. 142–149, 2022.
- [14] M. B. Wang and S. C. Li, "A complex variable solution for stress and displacement field around a lined circular tunnel at great depth," *International Journal for Numerical and Analytical Methods in Geomechanics*, vol. 33, no. 7, pp. 939–951, 2009.
- [15] P. Li, Y. Zhao, D. Zhang, and J. Liu, "Elastic-plastic solution to the stress and deformation of deep circular tunnel with lining considering stress release," *China Railway Science*, vol. 34, no. 2, pp. 58–65, 2013.
- [16] A. R. Kargar, "An analytical solution for circular tunnels excavated in rock masses exhibiting viscous elastic-plastic behavior," *International Journal of Rock Mechanics and Mining Sciences*, vol. 124, p. 104128, 2019.
- [17] Z. Guo, B. Wu, and S. Jia, "An analytical model for predicting the mechanical behavior of a deep lined circular pressure tunnel by using complex variable method," *Geomechanics and Geophysics for Geo-Energy and Geo-Resources*, vol. 7, no. 4, pp. 90–28, 2021.
- [18] A. Kargar, R. Rahmamejad, and M. Hajabasi, "A semi-analytical elastic solution for stress field of lined non-circular tunnels at great depth using complex variable method," *International Journal of Solids and Structures*, vol. 51, no. 6, pp. 1475–1482, 2014.
- [19] A. R. Kargar, R. Rahmamejad, and M. A. Hajabasi, "The stress state around lined non-circular hydraulic tunnels below the water table using complex variable method," *International Journal of Rock Mechanics and Mining Sciences*, vol. 78, pp. 207–216, 2015.
- [20] A. Z. Lu, N. Zhang, and Y. Qin, "Analytical solutions for the stress of a lined non-circular tunnel under full-slip contact conditions," *International Journal of Rock Mechanics and Mining Sciences*, vol. 79, pp. 183–192, 2015.
- [21] A. Z. Lu, N. Zhang, and L. Kuang, "Analytic solutions of stress and displacement for a non-circular tunnel at great depth including support delay," *International Journal of Rock Mechanics and Mining Sciences*, vol. 70, pp. 69–81, 2014.
- [22] S. Wang, A. Lu, and X. Zhang, "Analytical solution for the non-circular hydraulic tunnel buried in the orthotropic rock mass," *Rock and Soil Mechanics*, vol. 39, no. 12, pp. 4437–4447+4456, 2018.
- [23] Y. Li and S. Chen, "A complex variable solution for lining stress and deformation in a non-circular deep tunnel II practical application and verification," *Mathematical and Computational Applications*, vol. 23, no. 3, p. 43, 2018.
- [24] Y. Li and S. Chen, "Lining and surrounding rock in non-circular tunnel based on complex variable method," *Journal of Southwest Jiaotong University*, vol. 55, no. 2, pp. 265–272, 2020.
- [25] S. Liu, P. Zhang, S. Chen, and Y. Zhu, "Stress and displacement of orthotropic surrounding rock with a deeply buried non-circular lined tunnel under the complete contact interface condition," *Journal of Mechanical Engineering*, vol. 57, no. 23, pp. 149–159, 2021.
- [26] F. Q. Chen, L. B. Lin, and D. Y. Li, "Analytic solutions for twin tunneling at great depth considering liner installation and mutual interaction between geomaterial and liners," *Applied Mathematical Modelling*, vol. 73, pp. 412–441, 2019.
- [27] H. Fang, D. Zhang, Q. Fang, and M. Wen, "A generalized complex variable method for multiple tunnels at great depth considering the interaction between linings and surrounding rock," *Computers and Geotechnics*, vol. 129, p. 103891, 2021.
- [28] J. Zhou and X. A. Yang, "An analysis of the support loads on composite lining of deep-buried tunnels based on the Hoek-Brown strength criterion," *Tunnelling and Underground Space Technology*, vol. 118, p. 104174, 2021.
- [29] J. Zhou, X. Yang, J. Cai, and F. Yang, "Distribution rules and mechanical solutions of loads on composite linings in deep-buried tunnels," *Chinese Journal of Rock Mechanics and Engineering*, vol. 40, no. 5, pp. 1009–1021, 2021.
- [30] J. Zhou, X. A. Yang, M. J. Ma, and L. H. Li, "The support load analysis of deep-buried composite lining tunnel in rheological rock mass," *Computers and Geotechnics*, vol. 130, p. 103934, 2021.
- [31] F. Li, N. Chang, J. Wang, T. Feng, and C. Li, "Research on the algorithm for composite lining of deep buried water conveyance tunnel," *Advances in Civil Engineering*, vol. 2021, Article ID 6686360, 14 pages, 2021.
- [32] S. Ramadan, M. H. El Naggar, O. Drbe, and K. Embaby, "Preliminary analysis and instrumentation of large-span three-sided reinforced concrete culverts," *Journal of Bridge Engineering*, vol. 27, no. 2, p. 4021105, 2022.
- [33] T. Maleska and D. Beben, "Numerical analysis of a soil-steel bridge during backfilling using various shell models," *Engineering Structures*, vol. 196, p. 109358, 2019.
- [34] K. Embaby, M. Hesham El Naggar, and M. El Sharnouby, "Investigation of bevel-ended large-span soil-steel structures," *Engineering Structures*, vol. 267, p. 114658, 2022.
- [35] T. Maleska, J. Nowacka, and D. Beben, "Application of EPS geofoam to a soil-steel bridge to reduce seismic excitations," *Geosciences*, vol. 9, no. 10, p. 448, 2019.
- [36] T. Maleska and D. Beben, "Behaviour of soil-steel composite bridge with various cover depths under seismic excitation," *Steel and Composite Structures*, vol. 42, no. 6, pp. 747–764, 2022.
- [37] Y. Shen, Z. Zhong, L. Li, X. Du, and M. Hesham El Naggar, "Seismic response of shield tunnel structure embedded in soil

- deposit with liquefiable interlayer,” *Computers and Geotechnics*, vol. 152, p. 105015, 2022.
- [38] J. Jiang, M. H. El Naggar, W. Huang, C. Xu, K. Zhao, and X. Du, “Seismic vulnerability analysis for shallow-buried underground frame structure considering 18 existing subway stations,” *Soil Dynamics and Earthquake Engineering*, vol. 162, p. 107479, 2022.
- [39] J. Chen, C. Xu, H. M. El Naggar, and X. Du, “Seismic response analysis of rectangular prefabricated subway station structure,” *Tunnelling and Underground Space Technology*, vol. 131, p. 104795, 2023.
- [40] J. Fan, *Stress and Displacement of Deep-Buried Non-circular Composite Lining Tunnel*, Shijiazhuang Tiedao University, Shijiazhuang, China, 2022.
- [41] China Railway Eryuan Engineering Group Co Ltd, *TB 10003-2016 Code for Design of Railway Tunnel*, China Railway Publishing House, Beijing, China, 2016.